Supporting Information

Hydrogen-bonding enables two-dimensional metal/semiconductor tunable contacts approaching the quantum limit and the modified Schottky-Mott limit simultaneously

Dexing Liu, Ziyi Liu, Jiahao Zhu & Min Zhang[1*]

School of Electronic and Computer Engineering, Peking University, Shenzhen 518055, China.

Table of contents

[1]* Corresponding author.
E-mail address: zhangm@ece.pku.edu.cn (M. Zhang).

Supplementary Figures

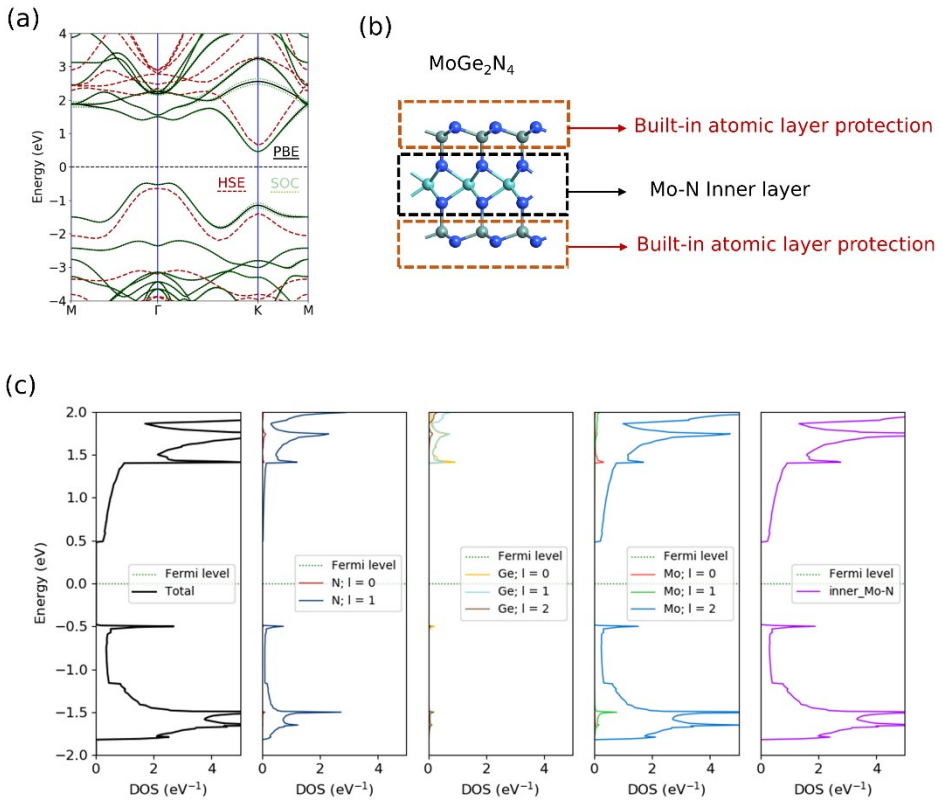

Fig. S1. Band structure and built-in atomic layer protection in monolayer $MoGe_2N_4$. (a) The band structure of MoGe2N4 monolayer calculated by PBE (black solid line), PBE+SOC (green dotted line) and HSE06 (red dashed line) methods, respectively. (b) The schematic of the built-in atomic layer protection in $MoGe_2N_4$. (c) The projected density of states (PDOS) of $MoGe_2N_4$. The conduction band bottom and valence band top of the $MoGe_2N_4$ are mainly composed of the Mo-N inner layer, which is protected by the outer atoms.

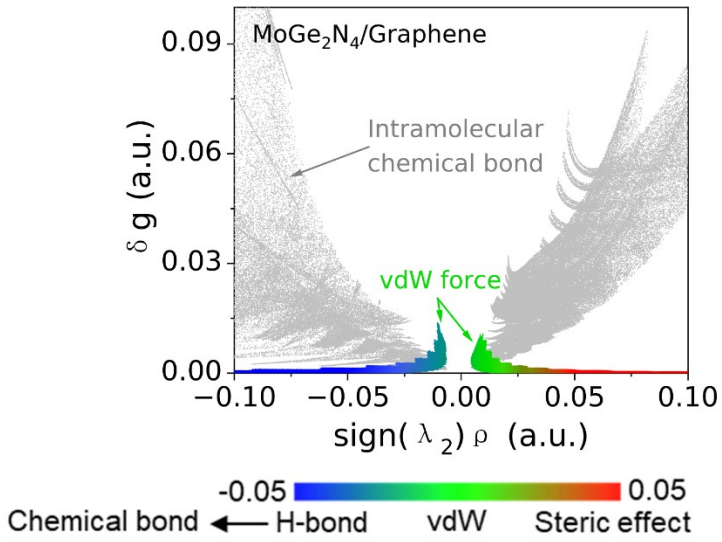

Fig. S2. The vdW contacts in $MoGe_2N_4$/Graphene junction as revealed by the independent gradient model (IGM) diagram. $sign(\lambda_2)\rho$ mapped 2D scatter plot of the electron density gradient difference (δg), where δg is divided into interlayer and intralayer interactions. The value of $sign(\lambda_2)\rho$ of interlayer interactions is represented by filling color according to the color bar, while the value of $sign(\lambda_2)\rho$ of intralayer interactions is represented by filling gray. ρ denotes the electron density at the weak interaction critical point, $sign(\lambda_2)$ denotes the sign of the second largest eigenvalue λ_2 of the electron density Hessian matrix. The $MoGe_2N_4$/Graphene junction is only bonded by the weak vdW forces.

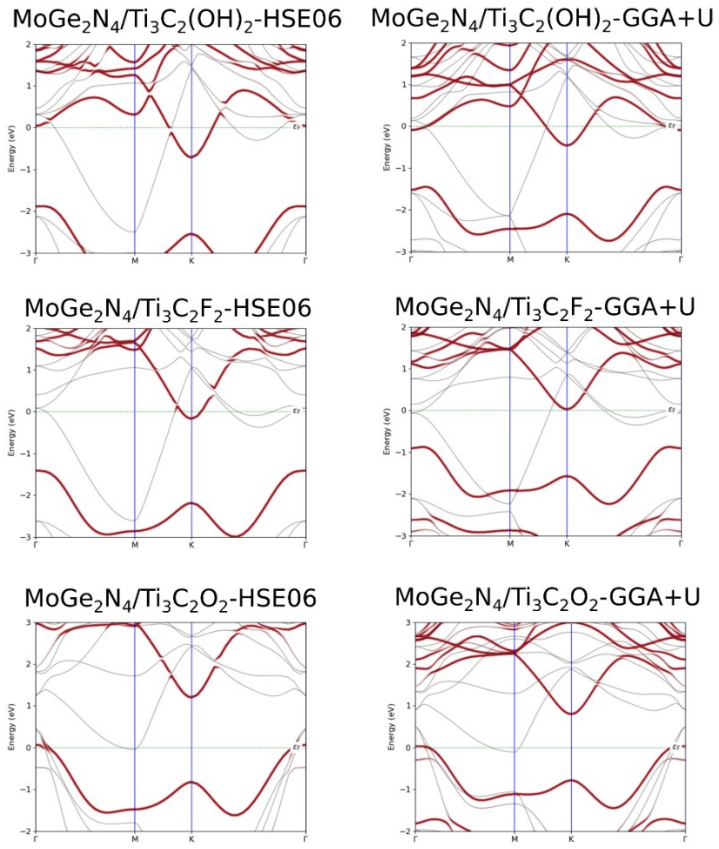

Fig. S3. Comparison of band structures calculated from HSE06 and GGA+U method. The band structures of $Ti_3C_2(OH)_2/MoGe_2N_4$, $Ti_3C_2F_2/MoGe_2N_4$, and $Ti_3C_2O_2/MoGe_2N_4$ junctions are shown from top to bottom. The hubbard U_{eff} value is set to 2.0 eV for Ti 3d orbitals, where U_{eff} = U−J with the exchange parameter J = 0.5 eV and the effective on-site Columbic repulsion parameter U = 2.5 eV, respectively. For $Ti_3C_2(OH)_2/MoGe_2N_4$ and $Ti_3C_2O_2/MoGe_2N_4$, GGA-PBE (Figs. 3e, h), GGA+U, and HSE06 method show consistent results, that is, $Ti_3C_2(OH)_2/MoGe_2N_4$ and $Ti_3C_2O_2/MoGe_2N_4$ can form N-type Ohmic contacts and P-type Ohmic contacts, respectively. And for $Ti_3C_2F_2/MoGe_2N_4$, N-type Ohmic contacts are obtained by the GGA+U and HSE06 method, while the GGA-PBE method yields Schottky contacts (Fig. 3g). The Fermi-level is set to zero.

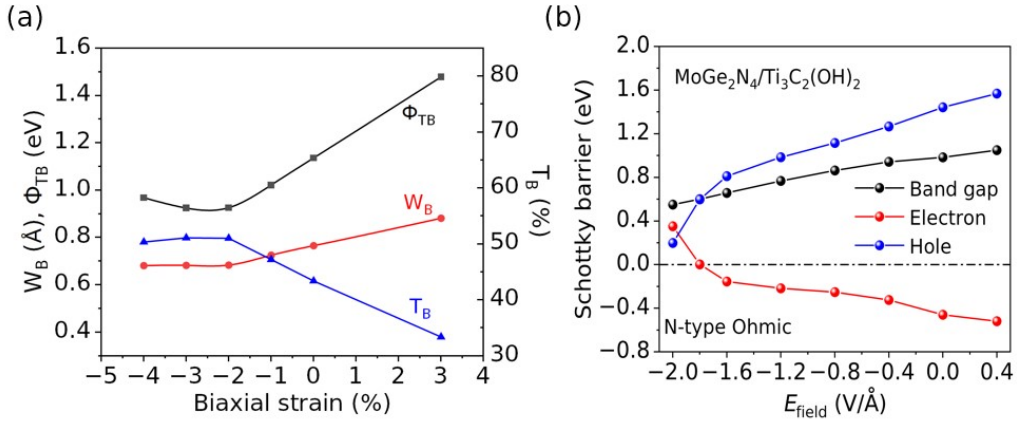

Fig. S4. (a) Effect of strain on the tunneling properties of $Ti_3C_2(OH)_2/MoGe_2N_4$ junction. The width (W_B) and height (ϕ_{TB}) of the tunnelling barrier and the probability of tunnelling (T_B) take extreme values at biaxial compressive strains of about -2%. **(b)Effect of electric field on Schottky barrier and band gap of $Ti_3C_2(OH)_2/MoGe_2N_4$ junction.** The direction from $MoGe_2N_4$ to $Ti_3C_2(OH)_2$ is defined as the positive direction of the electric field. The more negative electric field leads to a smaller hole Schottky barrier and band gap of the junction, while the electron Schottky barrier is larger. When the electric field strength is about -1.8 V/Å, the electron Schottky barrier changes from negative to positive, indicating the disappearance of the N-type Ohmic contact.

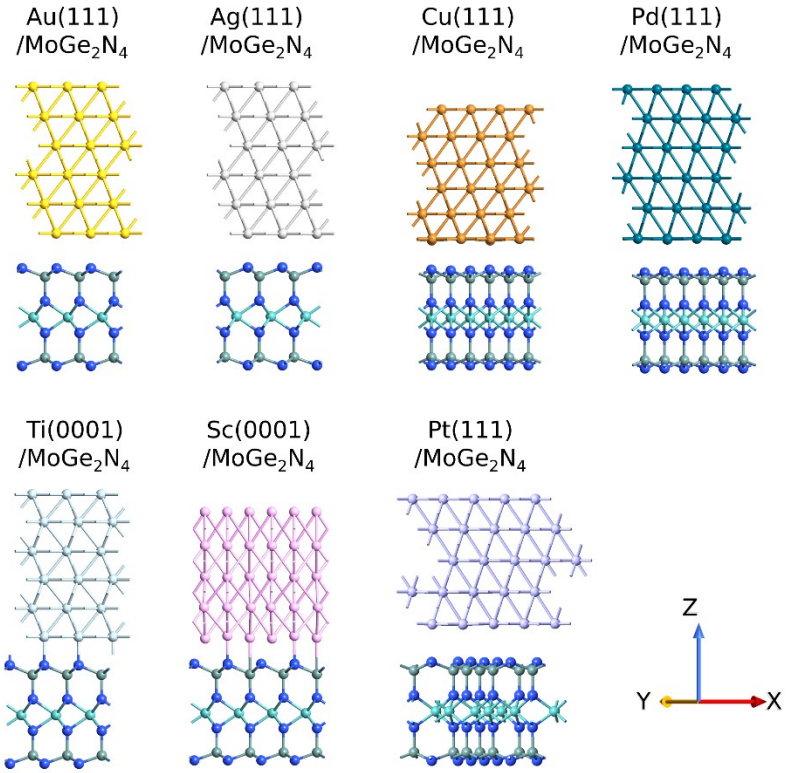

Fig. S5. Relaxed lattice structures of conventional metal/$MoGe_2N_4$ junctions. The contact surfaces of metals are selected based on their low surface free energy and thermodynamic stability. The metal/$MoGe_2N_4$ junctions are constructed by stretching the metal layer to match the lattice constant of $MoGe_2N_4$, and the lattice mismatches are all less than 5%.

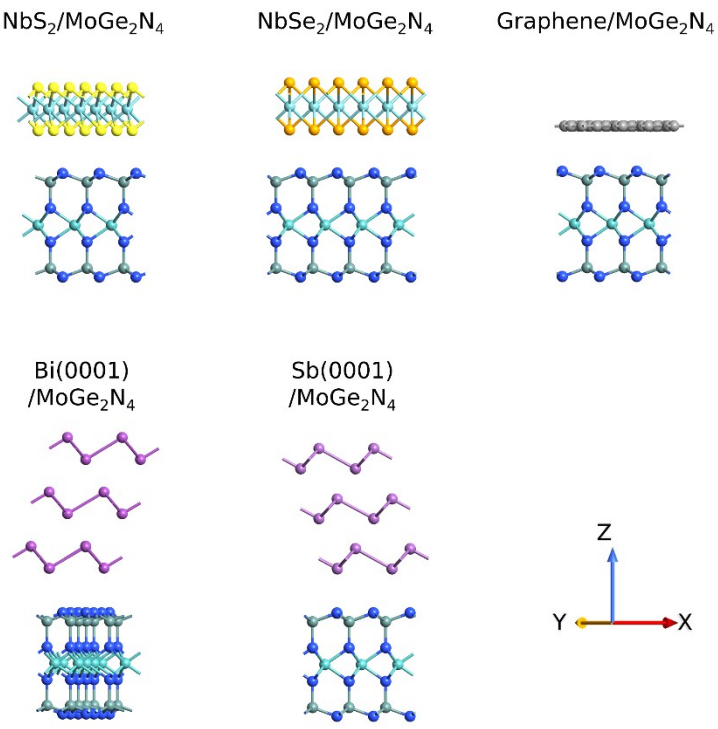

Fig. S6. Relaxed lattice structures of 2D vdW metal/$MoGe_2N_4$ junctions (top) and semimetal $MoGe_2N_4$ junctions (bottom). The metal/$MoGe_2N_4$ junctions are constructed by stretching the metal layer to match the lattice constant of $MoGe_2N_4$, and the lattice mismatches are all less than 5%.

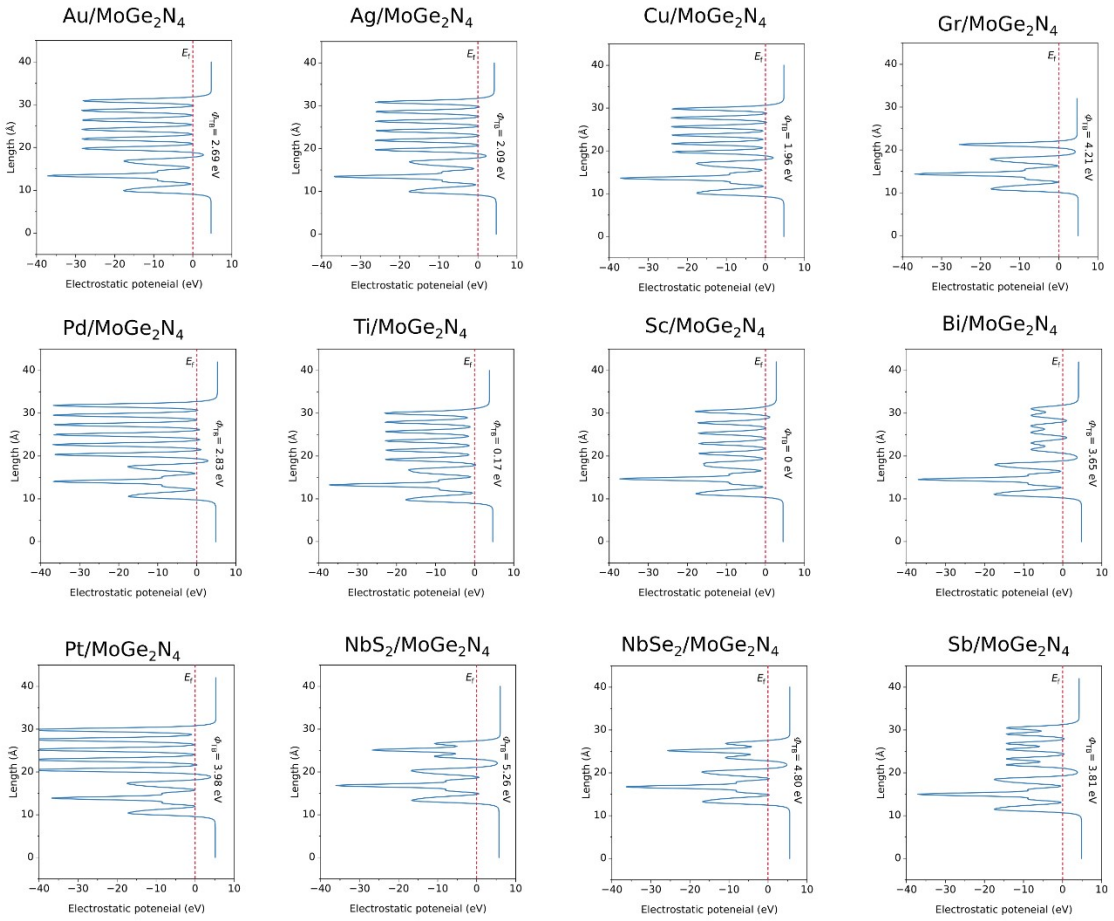

Fig. S7. The plane-averaged electrostatic potential along the z-direction of metal/ $MoGe_2N_4$ junctions. The tunneling barrier height ϕ_{TB} is marked in the Fig.s. The Fermi-level is set to zero.

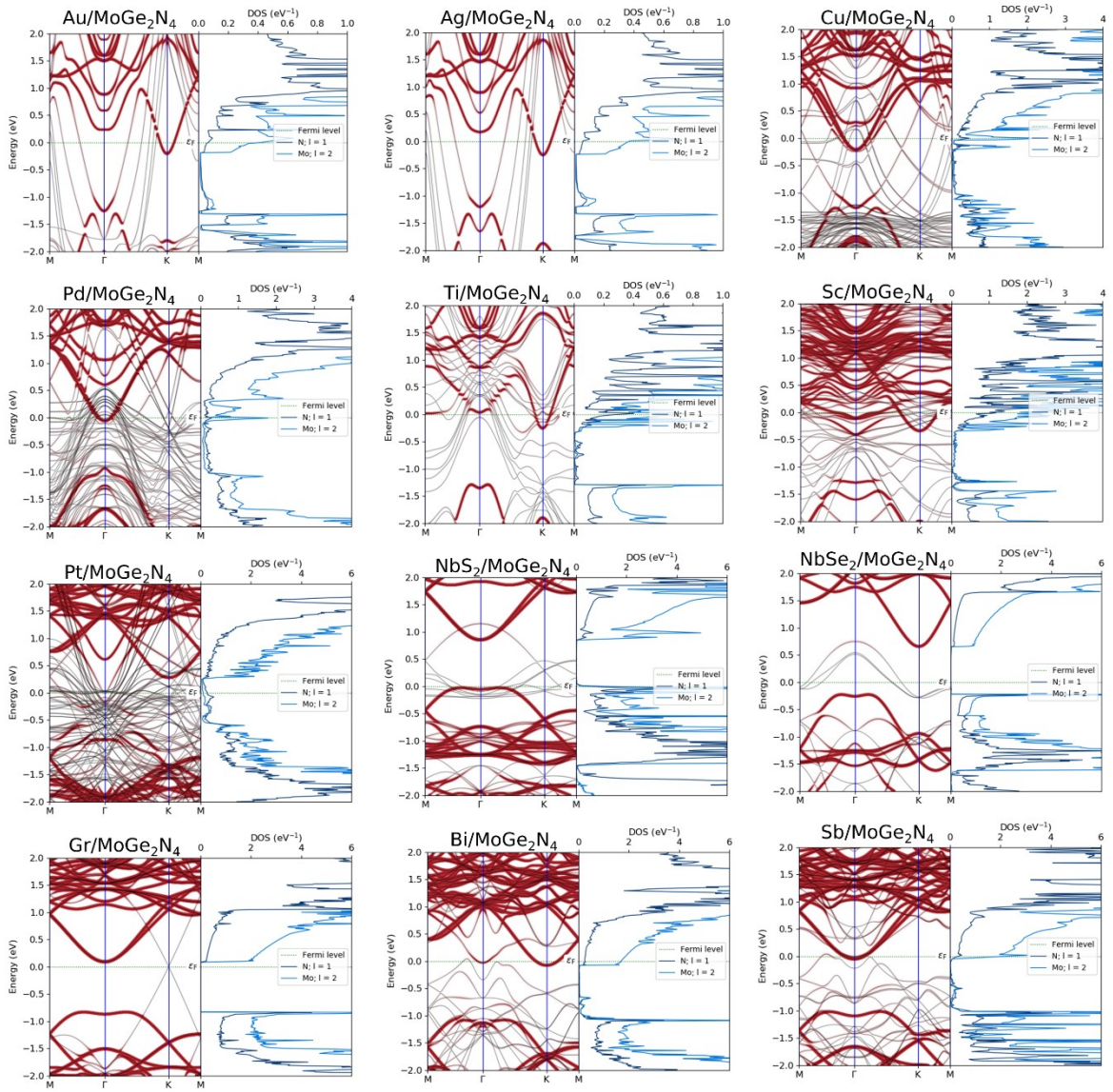

Fig. S8. The detailed electronic structures of various metal/$MoGe_2N_4$ junctions. The projections of $MoGe_2N_4$ are marked in red in the band structures, and the projections of d orbitals of Mo and p orbitals of N are marked in light blue and dark blue respectively in the PDOS. The Fermi-level is set to zero. Conventional metal contacts introduce metallic-induced gap states (MIGS) in the band gap, while MIGS is completely absent in 2D vdW contacts. In contrast, MIGS saturation occurs for semimetal Bi and Sb contacts.

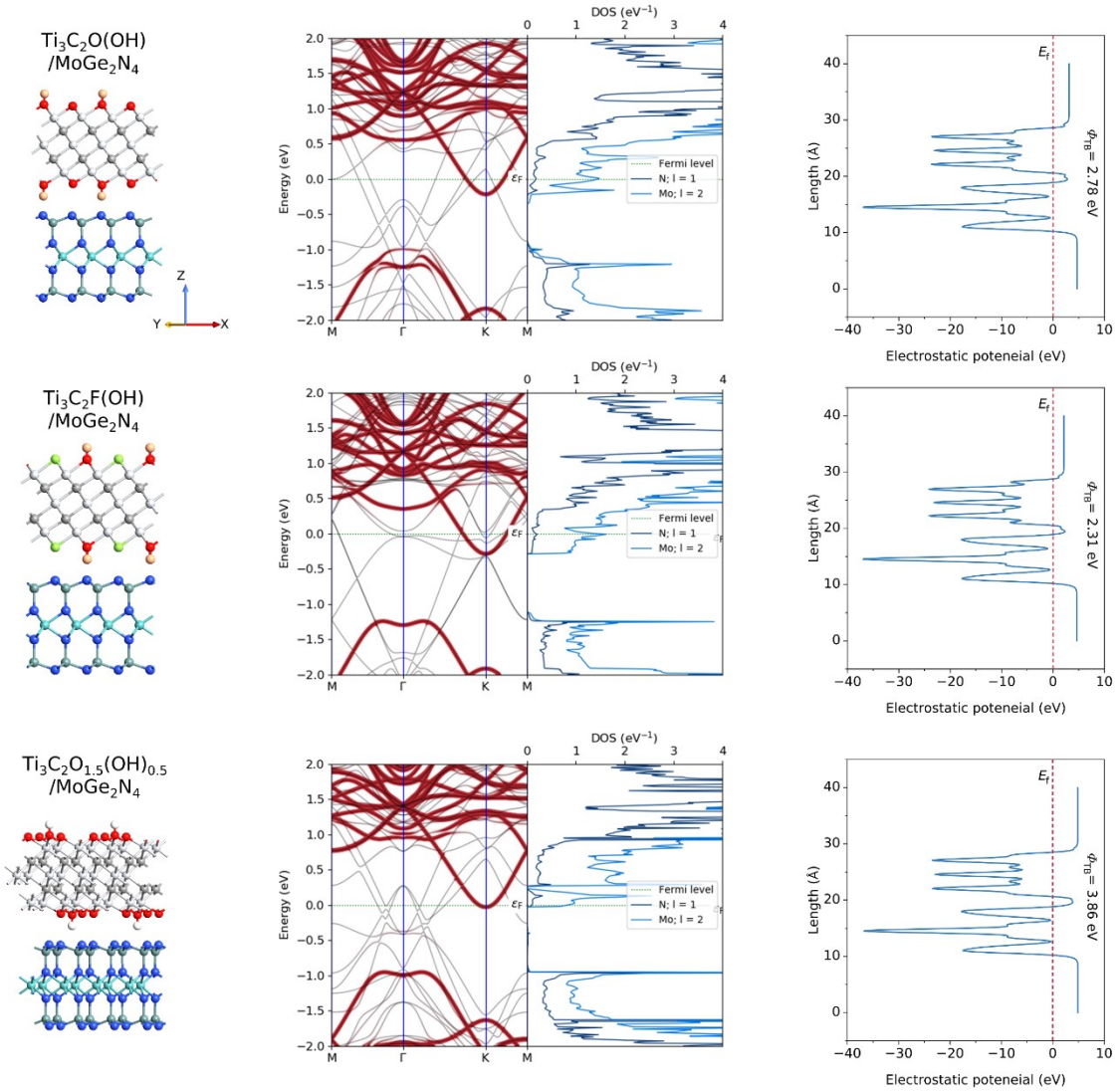

Fig. S9. Tunable hydrogen-bonding enhanced contacts in $Ti_3C_2O_xF_y(OH)_{2-x-y}$/ $MoGe_2N_4$ junctions. The relaxed lattice structures, electronic structures, and plane-averaged electrostatic potential along the z-direction of the junctions are shown from left to right. The Fermi-level is set to zero. The $Ti_3C_2O(OH)$ and $Ti_3C_2F(OH)$ with surface hydroxyl content of 50%, and $Ti_3C_2O_{1.5}(OH)_{0.5}$ with surface hydroxyl content of 25% are shown from top to bottom. As the surface hydroxyl content decreases the tunneling barrier height ϕ_{TB} rises accordingly.

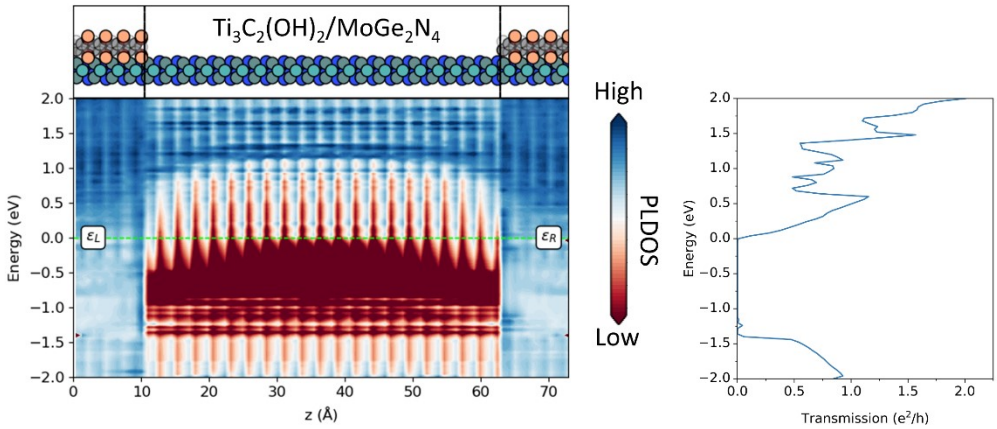

Fig. S10. Quantum transport properties of 5-nm $MoGe_2N_4$ FET with double-side $Ti_3C_2(OH)_2$ contacts. Projected local density of states (PLDOS) and transmission spectrum (including two spin channels) are shown on the left and right respectively. The Fermi-level is set to zero. The lateral Schottky barrier for double-side contacts is about -0.46 eV, which is consistent with the value for single-side contacts. Ultra-sharp contact interfaces indicate the damage-free properties of hydrogen-bonding contacts Transmission spectrum shows the existence of nearly-perfect conducting channels near the Fermi-level, showing good Ohmic contact properties.

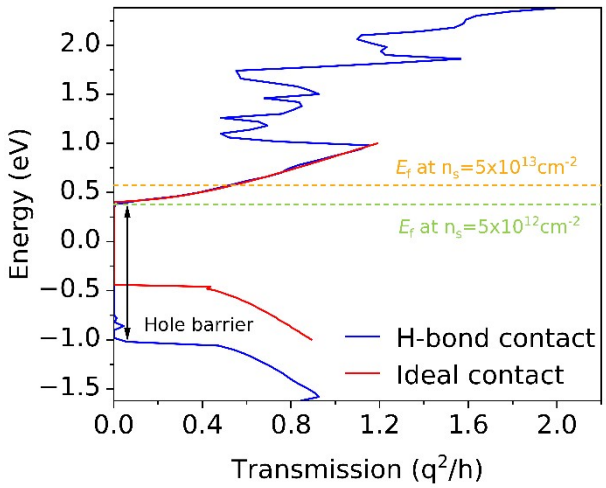

Fig. S11. Comparison of transmission spectra between $MoGe_2N_4$ FETs with hydrogen-bonding contact and with fully ideal contact. Due to the energy band bending and the enhancement of the hole Schottky barrier, the transmission gap of the hydrogen-bonding contact is broadened compared to the ideal transmission spectrum. The green and orange dashed lines indicate the Fermi energy levels at carrier concentrations of 5×10^{12} cm^{-2} and 5×10^{13}, respectively. The transmission spectrum near the bottom of the conduction band of hydrogen-bonding contact perfectly reproduces the ideal ballistic transport spectrum.

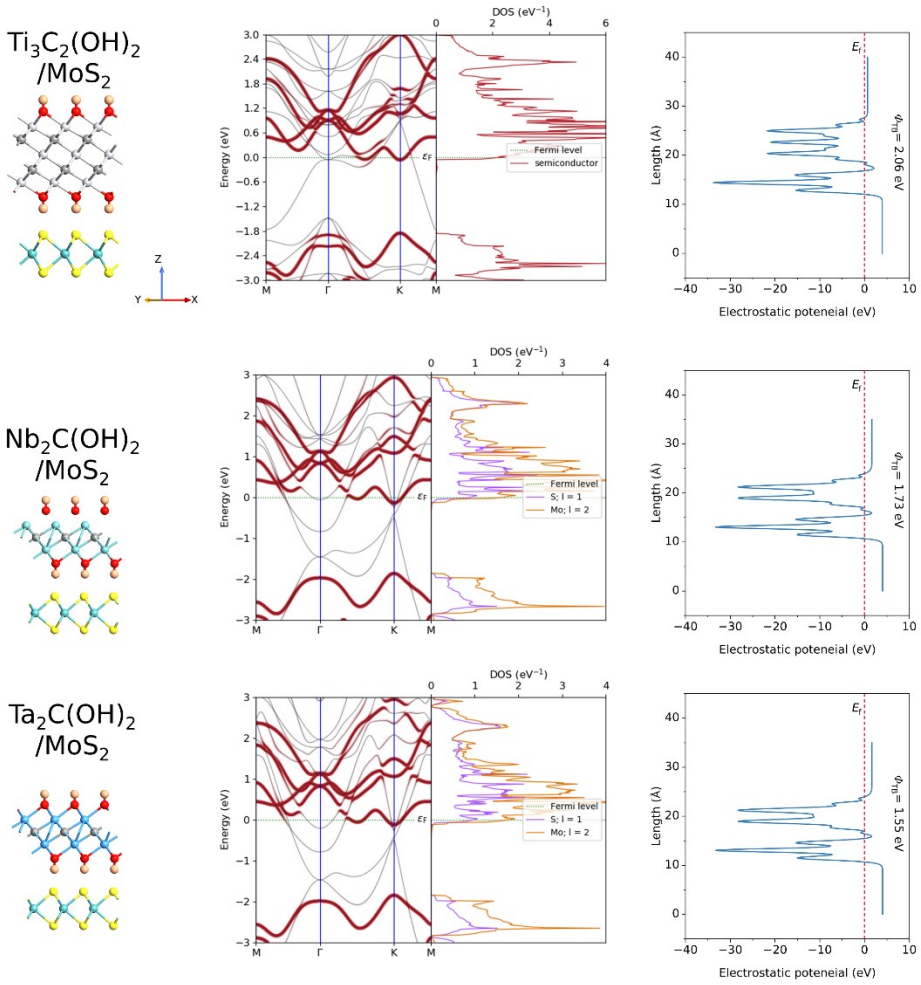

Fig. S12. Performance comparison between $Ti_3C_2(OH)_2/MoS_2$, (top), $Nb_2C(OH)_2/MoS_2$ (middle), and $Ta_2C(OH)_2/MoS_2$ (bottom) contacts. The relaxed lattice structures, electronic structures, and plane-averaged electrostatic potential along the z-direction of the junctions are shown from left to right. The Fermi-level is set to zero. All three systems form N-type Ohmic contacts and have clean interfaces without MIGS.

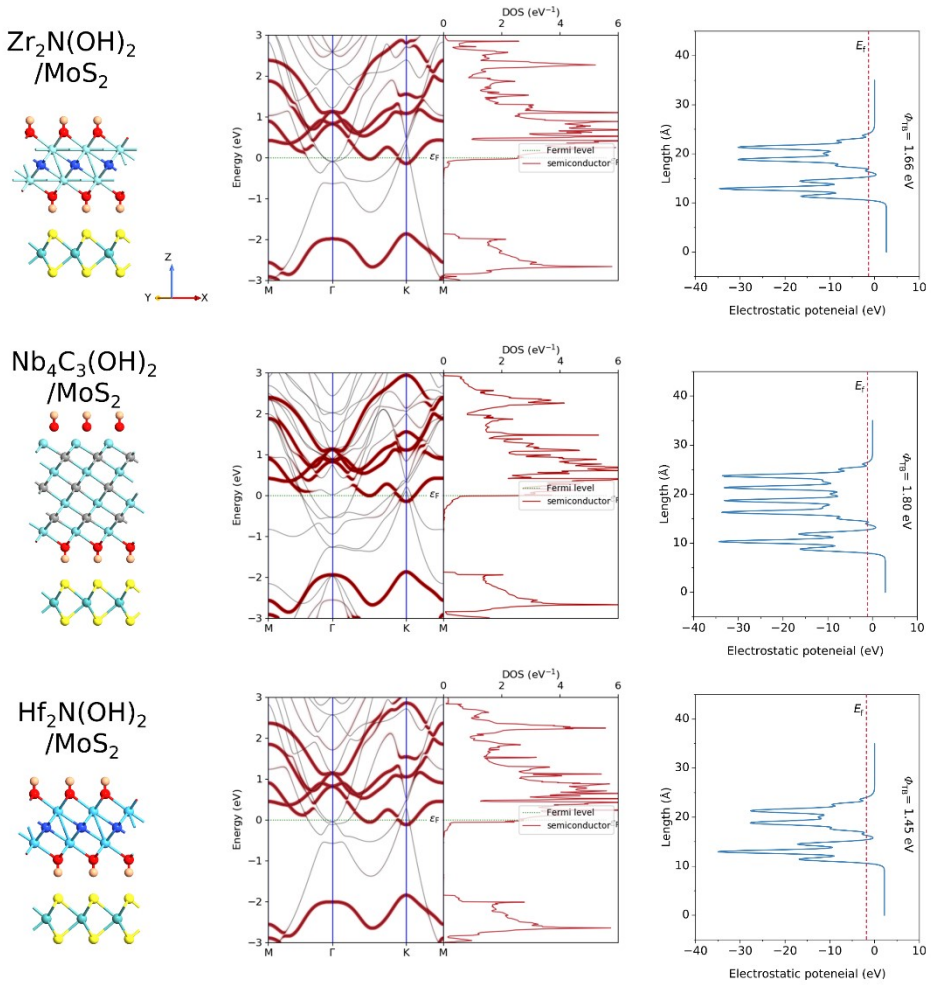

Fig. S13. Performance comparison between $Zr_2N(OH)_2/MoS_2$, (top), $Nb_4C_3(OH)_2/MoS_2$ (middle), and $Hf_2N(OH)_2/MoS_2$ (bottom) contacts. The relaxed lattice structures, electronic structures, and plane-averaged electrostatic potential along the z-direction of the junctions are shown from left to right. The Fermi-level is set to zero. All three systems form N-type Ohmic contacts and have clean interfaces without MIGS. The hydrogen-bonding formed in $Hf_2N(OH)_2/MoS_2$ has the closest contact.

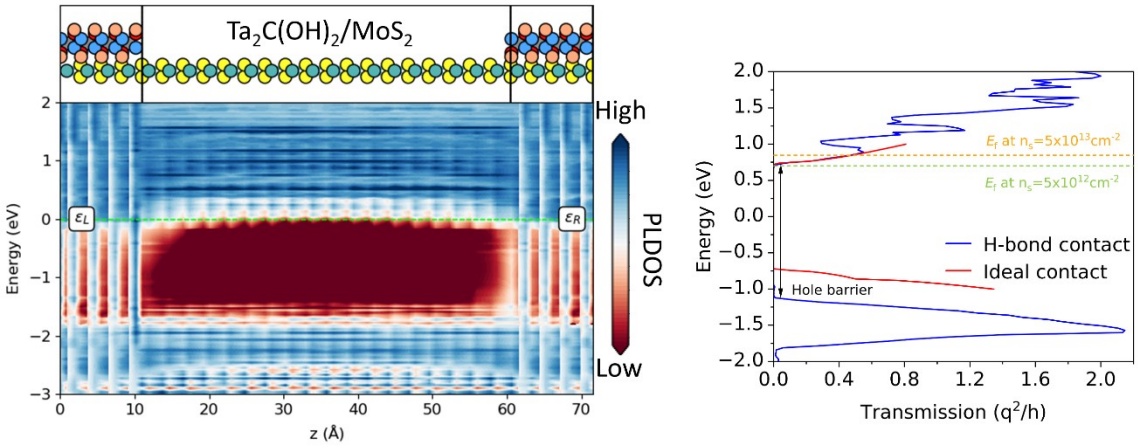

Fig. S14. Quantum transport properties of 5-nm MoS_2 FET with double-side $Ta_2C(OH)_2$ contacts. PLDOS and transmission spectrum (including two spin channels) are shown on the left and right respectively. The negative lateral Schottky barrier means that the Schottky-barrier-free transport is achieved. The dispersed electronic states around the interfaces are due to the presence of unsaturated bonds at the interruption of the $Ta_2C(OH)_2$ lattice. Due to the energy band bending and the enhancement of the hole Schottky barrier, the transmission gap of the hydrogen-bonding contact is broadened compared to the ideal transmission spectrum. The green and orange dashed lines in transmission spectrum diagram indicate the Fermi energy levels at carrier concentrations of 5×10^{12} cm^{-2} and 5×10^{13} respectively. The transmission spectrum near the bottom of the conduction band of hydrogen-bonding contact perfectly reproduces the ideal ballistic transport spectrum.

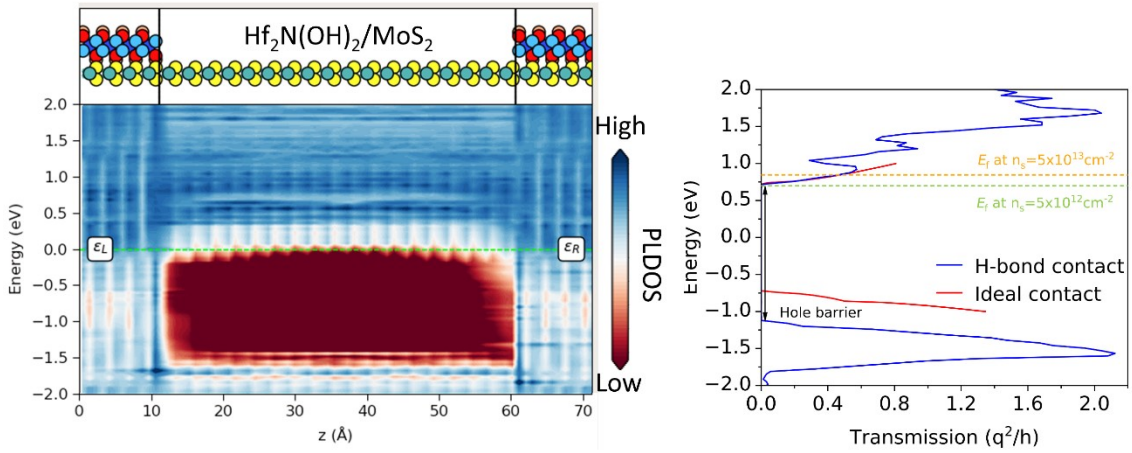

Fig. S15. Quantum transport properties of 5-nm MoS_2 FET with double-side $Hf_2N(OH)_2$ contacts. PLDOS and transmission spectrum (including two spin channels) are shown on the left and right respectively. The negative lateral Schottky barrier means that the Schottky-barrier-free transport is achieved. The dispersed electronic states around the interfaces are due to the presence of unsaturated bonds at the interruption of the $Hf_2N(OH)_2$ lattice. Due to the energy band bending and the enhancement of the hole Schottky barrier, the transmission gap of the hydrogen-bonding contact is broadened compared to the ideal transmission spectrum. The green and orange dashed lines in transmission spectrum diagram indicate the Fermi energy levels at carrier concentrations of 5×10^{12} cm^{-2} and 5×10^{13} respectively. The transmission spectrum near the bottom of the conduction band of hydrogen-bonding contact perfectly reproduces the ideal ballistic transport spectrum.

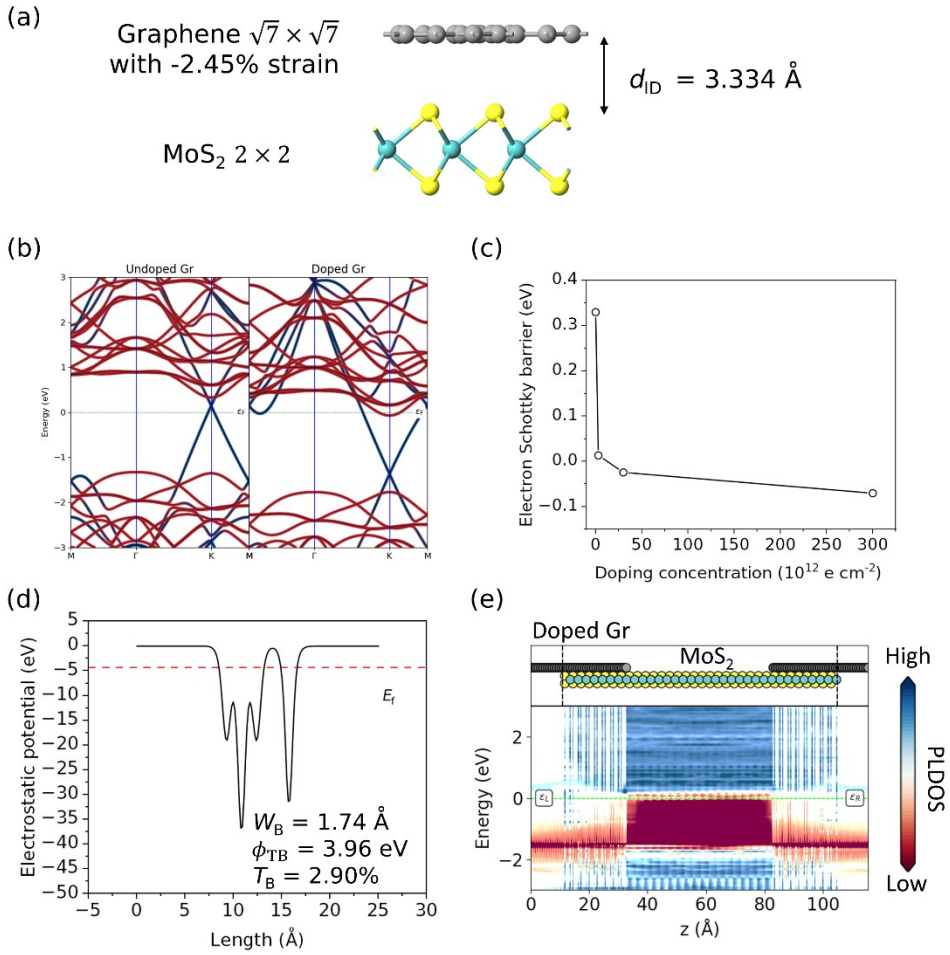

Fig. S16. vdW contact between doped graphene (Gr) and MoS_2. (a) Slab model for Gr/MoS_2 heterojunction and equilibrium spacing distance. (b) Projected energy bands of Gr/MoS_2 heterojunction. The contribution of MoS_2 is projected in red and the contribution of Gr is projected in blue. The doping concentration of the doped Gr is 3×10^{14} e cm^{-2}. (c) Electron Schottky barrier as a function of doping concentration of Gr. (d) Plane-averaged electrostatic potential along the z-direction of the Gr/MoS_2 heterojunction. (e) PLDOS of 5 nm MoS_2 FET with 2 nm doped Gr (n = 3×10^{14} e cm^{-2}) contact. The carrier concentration of MoS_2 is 3×10^{13} cm^{-2}.

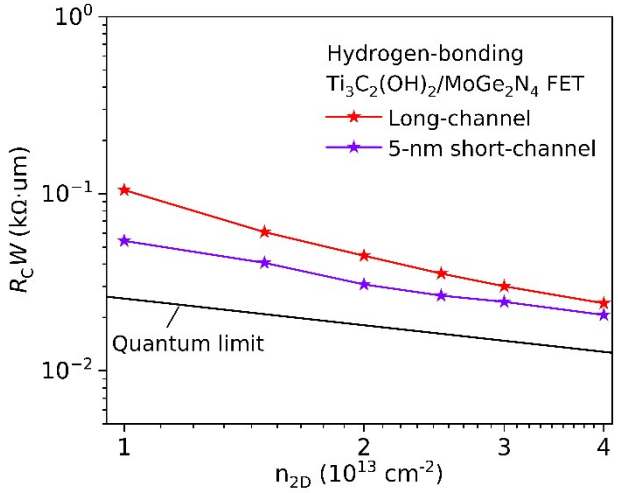

Fig. S17. Comparison of the contact resistance as a function of gate-induced carrier concentration of $Ti_3C_2(OH)_2/MoGe_2N_4$ based long-channel FETs with short-channel FETs with 5-nm channel length. Lower contact resistances in short-channel devices due to the heavy doping effect of $Ti_3C_2(OH)_2$ electrodes.

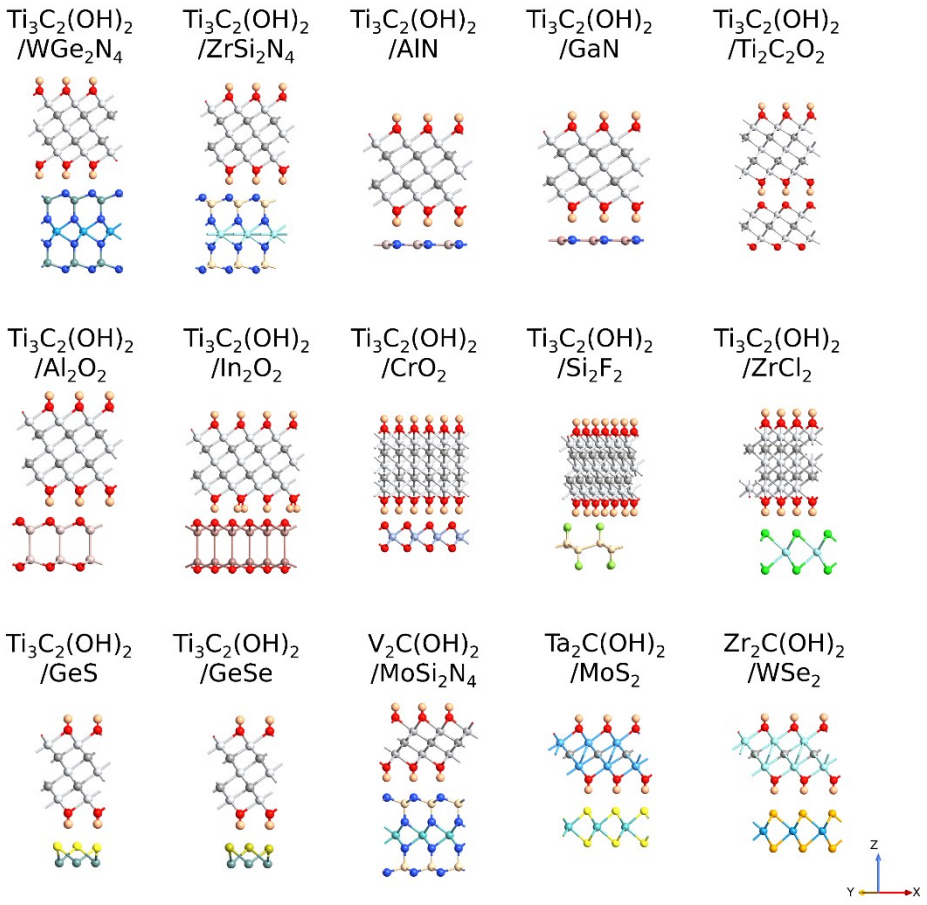

Fig. S18. Relaxed lattice structures of various hydrogen-bonding M/S junctions. The M/S junctions are constructed by stretching the metal layer to match the lattice constant of semiconductor, and the lattice mismatches are all less than 5%.

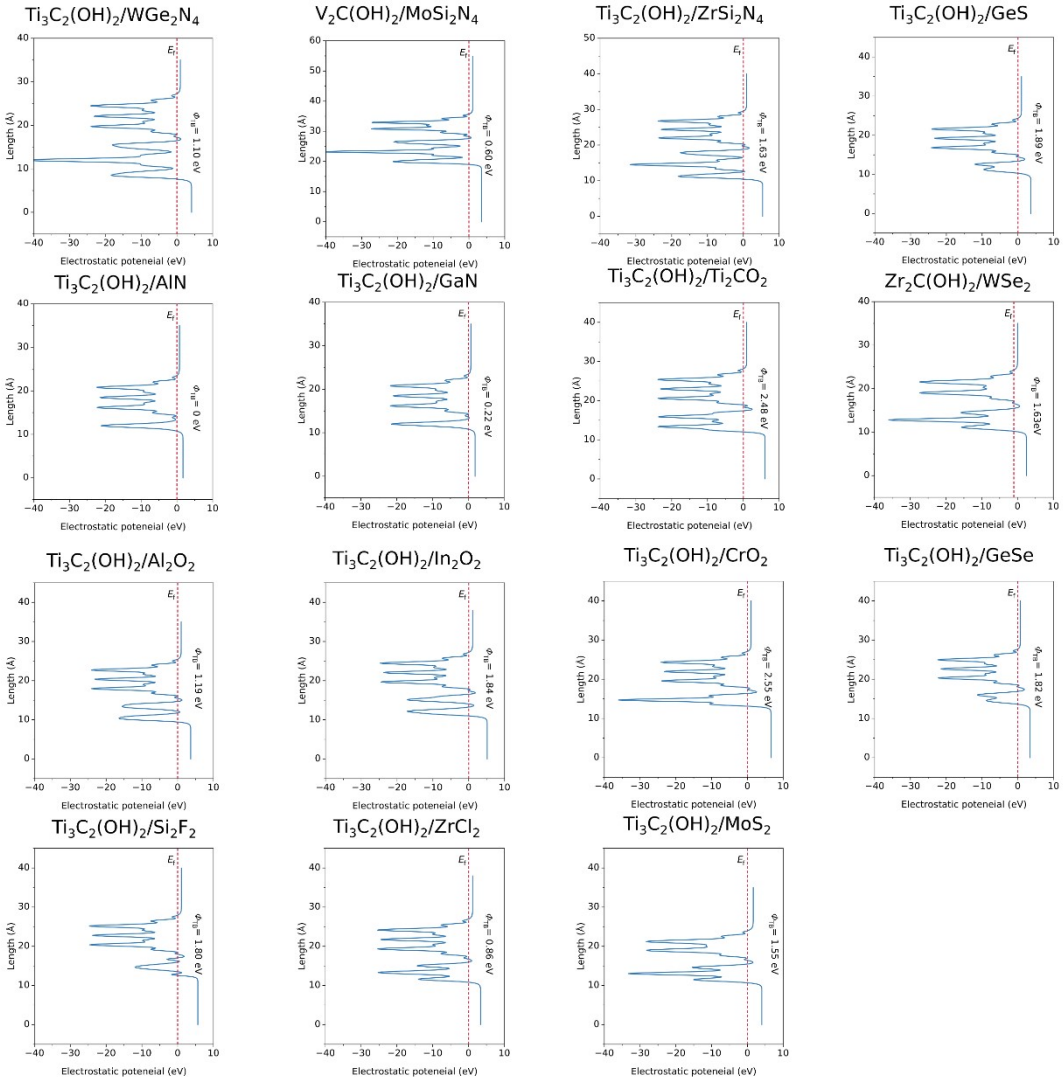

Fig. S19. The plane-averaged electrostatic potential along the z-direction of various hydrogen-bonding junctions. The tunneling barrier height ϕ_{TB} is marked in the figure. The Fermi-level is set to zero. Hydrogen-bonding contacts exhibit high tunneling efficiency due to the small tunneling barrier.

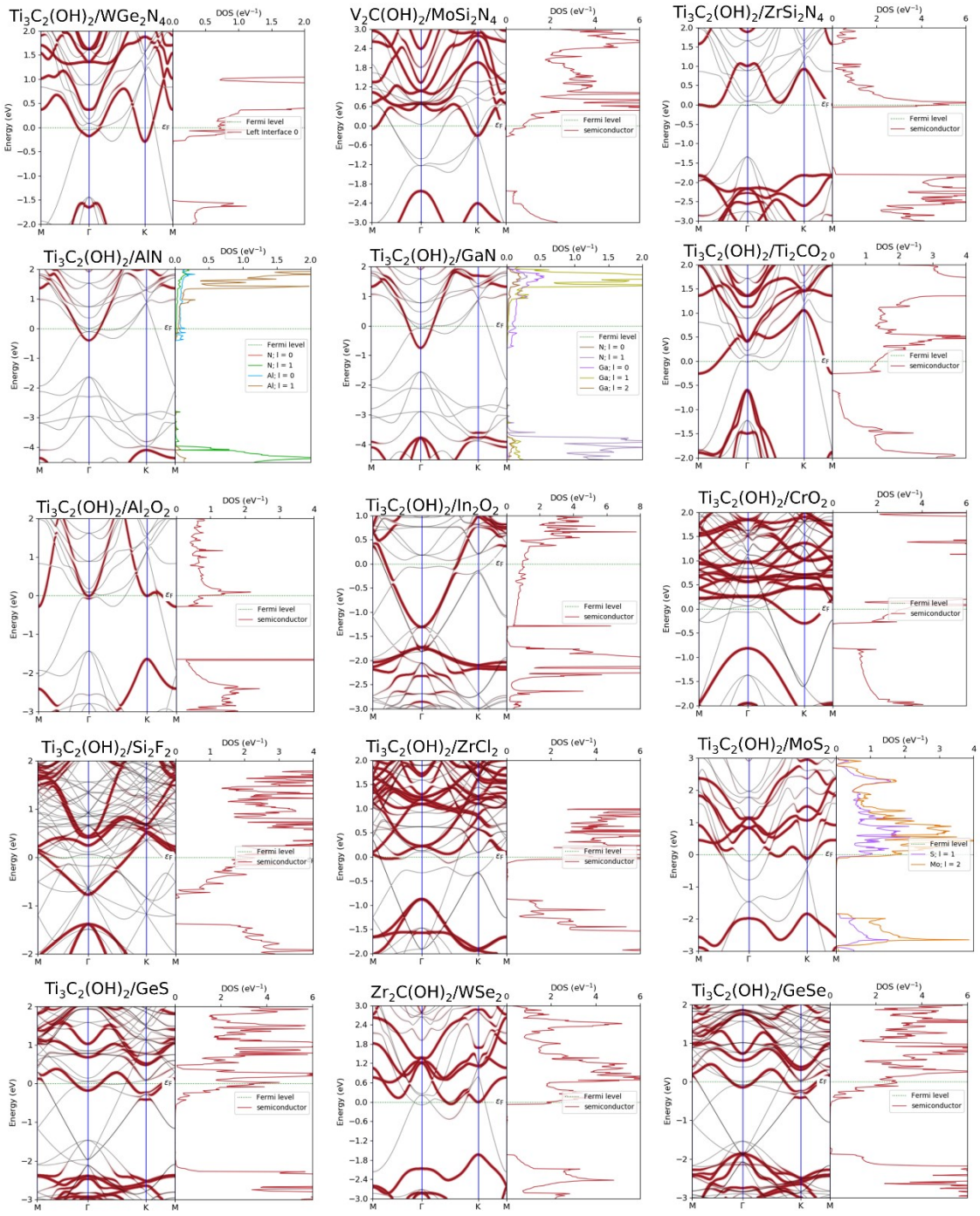

Fig. S20. The Detailed electronic structures of various hydrogen-bonding junctions. The projections of semiconductor are marked in red in the band structures and PDOS. The Fermi-level is set to zero. All combinations form N-type Ohmic contacts and have clean interfaces without MIGS.

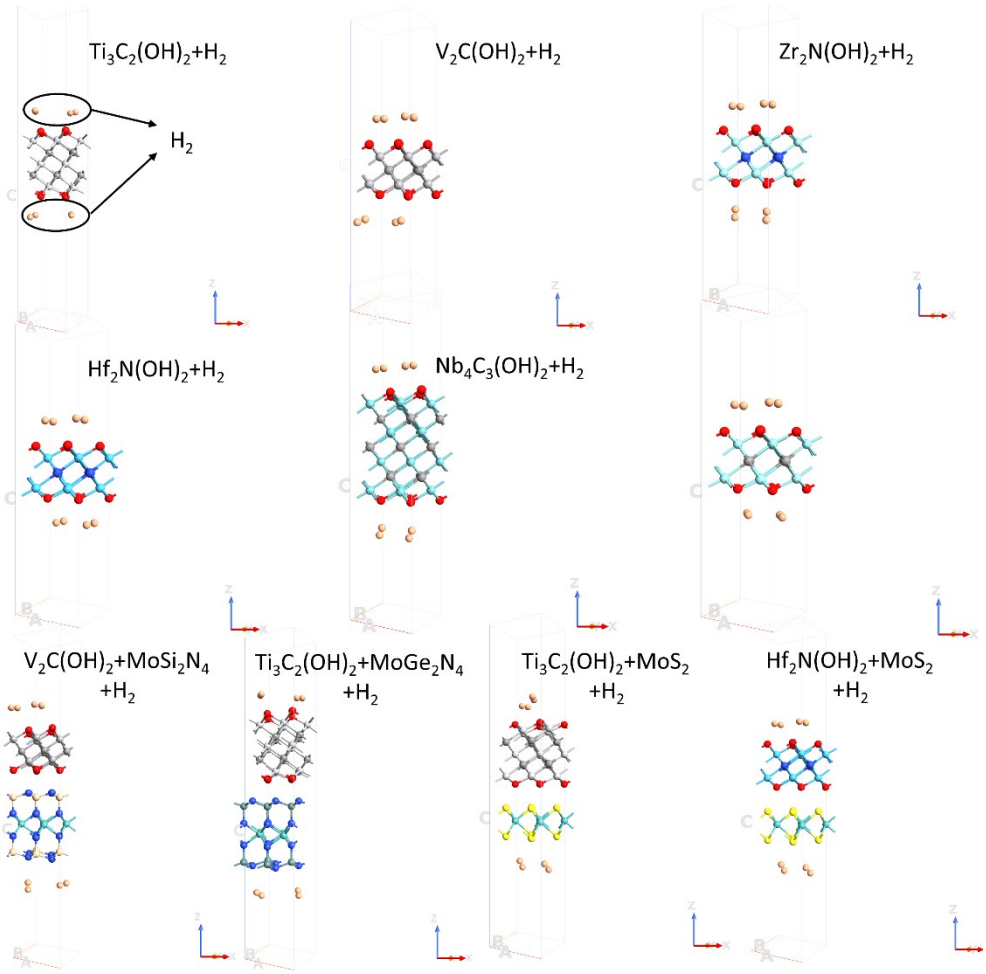

Fig. S21. Relaxed lattice structures of various dehydrogenated MXenes and hydrogen-bonding M/S junctions. Each model contains four H_2 molecules. The H-H bond length of the H_2 molecule is calculated to be 0.75 Å.

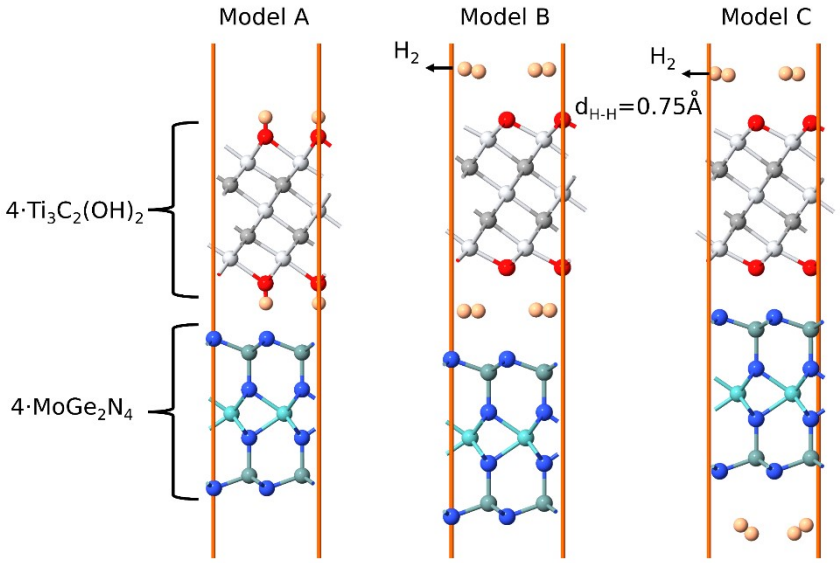

Configurations	Energy (eV)	Energy relative to Model A (eV)
Model A	-56083.60654	0
Model B	-56081.57241	2.03413
Model C	-56082.75609	0.85045

Fig. S22. Relaxed lattice structures of $Ti_3C_2(OH)_2/MoGe_2N_4$ heterojunction (model A) and its two dehydrated products (Model B and C). The table below shows a comparison of the energies of the three models.

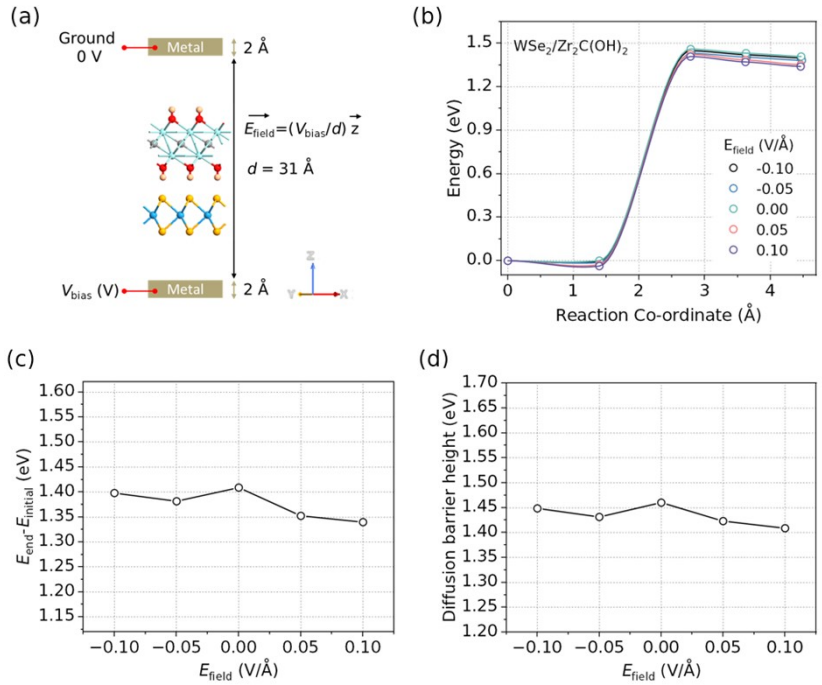

Fig. S23. Effect of electric field on diffusion barriers. (a) The slab model of $WSe_2/Zr_2C(OH)_2$ that takes into account the action of the electrostatic field. (b) Calculated diffusion pathways for one H-atom transferred from $Zr_2C(OH)_2$ to WSe_2 as a function of electric field strength. (c) Calculated energy difference (E_{end}-$E_{initial}$) for the transfer process of one H-atom as a function of electric field strength. (d) Calculated diffusion barriers for one H-atom transferred from $Zr_2C(OH)_2$ to WSe_2 as a function of electric field strength. The results show that electric fields in the range of -0.1 V/ Å to 0.1 V/ Å have a limited influence on the diffusion barriers of H atoms, whereas the electric field strength of a practically operated 2D transistor is about 10^{-4}-10^{-3} V/Å.

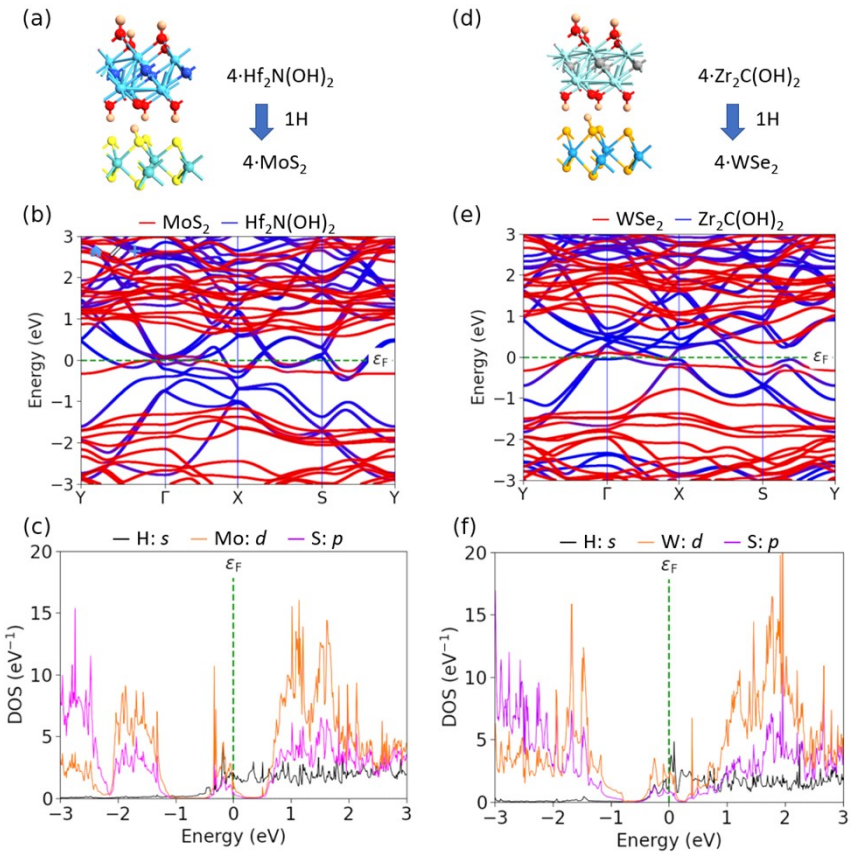

Fig. S24. Geometric and electronic structures of (a)-(c) $Hf_2N(OH)_2/MoS_2$ and (d)-(e) $Zr_2C(OH)_2/WSe_2$ heterojunctions after H-atom transfer occurs. The heterojunction is modelled as a supercell containing 4 MoS_2 (WSe_2) and 4 $Hf_2N(OH)_2$ ($Zr_2C(OH)_2$), where an H atom is transferred from MoS_2 (WSe_2) to $Hf_2N(OH)_2$ ($Zr_2C(OH)_2$). The projected energy bands and projected density of states indicate that MoS_2 (WSe_2) adsorbs an H atom and thus transforms into a semimetal.

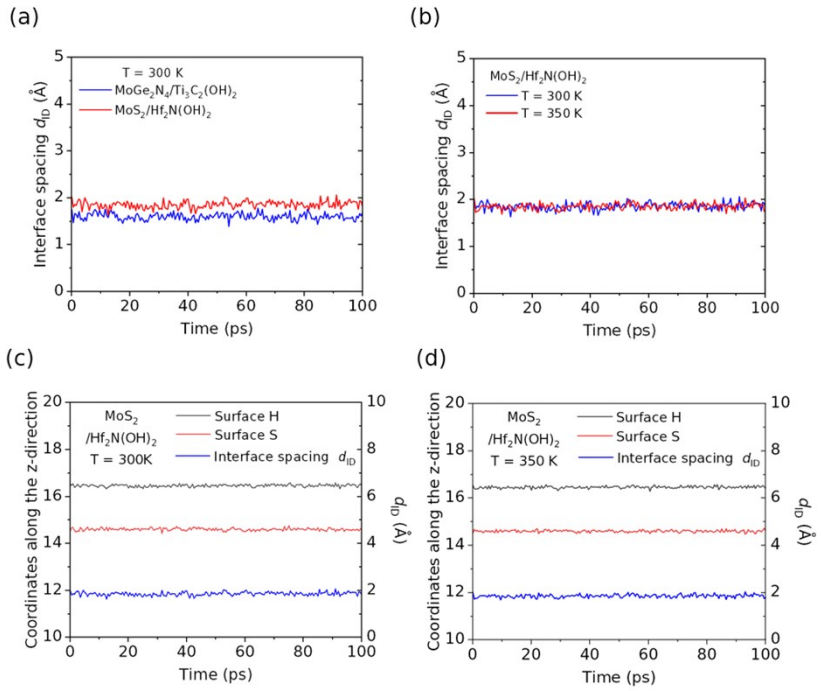

Fig. S25. Evolution of interfacial spacing with time for two typical hydrogen-bonding heterojunctions at different temperatures. (a) Interfacial spacing of $MoGe_2N_4/Ti_3C_2(OH)_2$ and $MoS_2/Hf_2N(OH)_2$ as a function of time at 300 K. (b) Interfacial spacing of $MoS_2/Hf_2N(OH)_2$ as a function of time at 300 K and 350 K, respectively. (c)-d) The interfacial S-atom z-axis coordinates, H-atom z-axis coordinates, and minimum interfacial spacing of $MoS_2/Hf_2N(OH)_2$ as a function of time at 300 K (c) and 350 K (d) respectively.

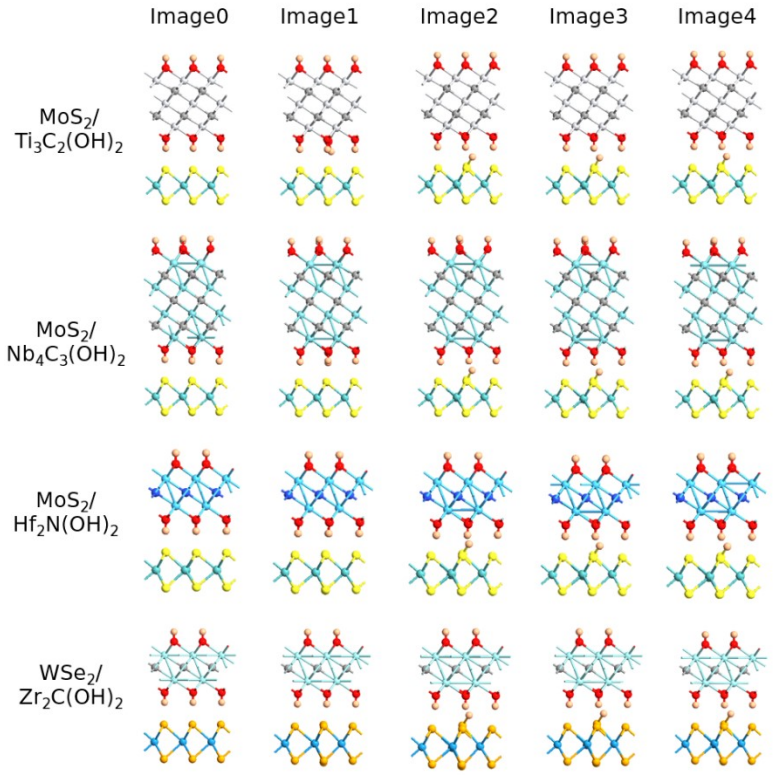

Fig. S26. Geometric and electronic structures of (a)-(c) $Hf_2N(OH)_2/MoS_2$ and (d)-(e) $Zr_2C(OH)_2/WSe_2$ heterojunctions after H-atom transfer occurs. The heterojunction is modelled as a supercell containing 4 MoS_2 (WSe_2) and 4 $Hf_2N(OH)_2$ ($Zr_2C(OH)_2$), where an H atom is transferred from MoS_2 (WSe_2) to $Hf_2N(OH)_2$ ($Zr_2C(OH)_2$). The projected energy bands and projected density of states indicate that MoS_2 (WSe_2) adsorbs an H atom and thus transforms into a semimetal.

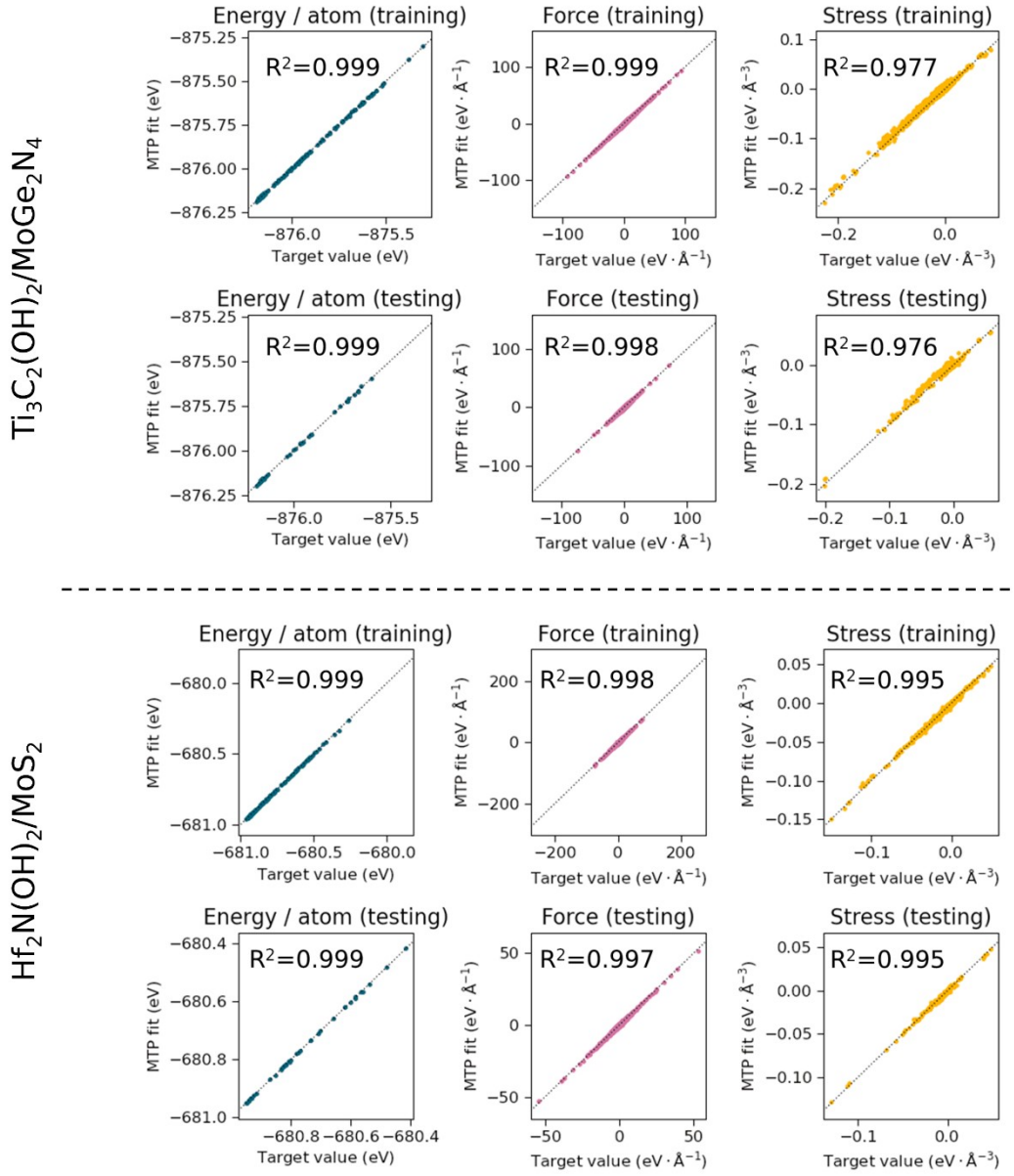

Fig. S27. Training and testing of machine learned moment tensor potential for $Ti_3C_2(OH)_2/MoGe_2N_4$ and $Hf_2N(OH)_2/MoS_2$. The total number of samples is slightly more than 200, where the ratio of training set to test set is 4:1.

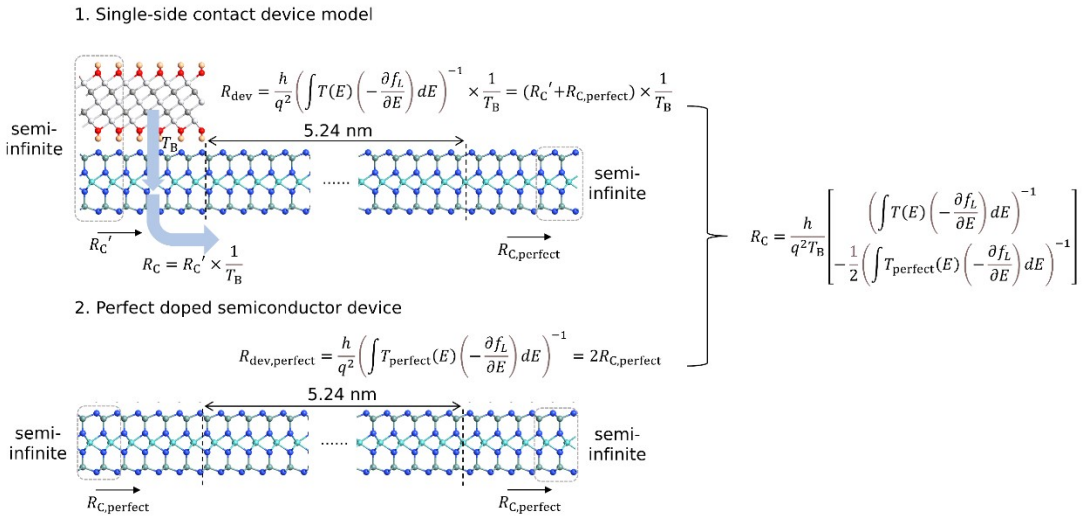

Fig. S28. Schematic illustration of calculating contact resistance (R_C) using single-side contact device model. The single-side contact device model contains the source of the MXene top contact, the scattering region, and the perfect doped semiconductor drain. The MXene contact derived R_C is therefore calculated by subtracting the total device resistance R_{dev} from the contact resistance at drain, which is obtained from a perfect doped semiconductor device.

Supplementary Tables

Different stacking configurations for $Ti_3C_2T_2/MoGe_2N_4$ junctions

Configurations		AA	AB	AC	AA*	AB*	AC*
$Ti_3C_2(OH)_2$/ $MoGe_2N_4$	E_b	-95.80	-67.89	-75.80	**-96.52**	-68.41	-59.12
	d_{ID}	1.77	2.01	1.83	1.76	2.01	1.83
$Ti_3C_2O_2$/ $MoGe_2N_4$	E_b	-41.16	-58.60	-57.18	-38.17	**-60.47**	-42.88
	d_{ID}	2.88	2.40	2.40	2.86	2.37	2.50
$Ti_3C_2F_2$/ $MoGe_2N_4$	E_b	-35.49	-48.73	-50.06	**-50.85**	-50.83	-47.40
	d_{ID}	2.83	2.38	2.30	2.33	2.34	2.36

Table S1. DFT calculated binding energy (E_b) and interfacial distance (d_{ID}) of different stacking configurations for $Ti_3C_2T_2/MoGe_2N_4$ junctions. The unit of E_b and d_{ID} is meV/Å^2 and Å respectively. The junction area A is 7.93 Å^2. The most stable configurations are marked in bold.

Conventional metal/$MoGe_2N_4$ contacts

Metal	**Au**	**Ag**	**Cu**	**Pd**	**Ti**	**Sc**	**Pt**
a_m	4.149	4.147	3.621	3.890	2.938	3.395	3.917
(h_1,h_2,h_3)	(111)	(111)	(111)	(111)	(0001)	(0001)	(111)
$a_{m/s}$	3.026	3.026	5.242	5.242	3.026	6.053	8.007
W_m	5.09	4.33	4.83	5.27	4.48	3.40	5.68
ε**(%)**	3.15	3.21	2.37	4.73	3.01	2.93	3.65
E_b	-64.51	-89.51	-88.27	-83.17	-159.83	-137.80	-57.01
d_{ID}	2.66	2.56	2.28	2.60	2.18	2.05	2.84
ϕ_{TB}	2.69	2.09	1.96	2.83	0.17	0	3.98
W_B	1.05	0.95	0.85	0.99	0.21	0	1.32
ΔV	-0.07	0.48	-0.03	-0.42	0.88	1.77	-0.11
ϕ_n	-0.21	-0.25	-0.21	-0.06	-0.26	-0.34	0.27
ϕ_p	0.99	1.02	1.03	0.93	1.29	1.25	0.72
E_g	0.78	0.77	0.82	0.87	1.03	0.91	1.00

Table S2. DFT calculated interfacial quantities for conventional metal/$MoGe_2N_4$ contacts. a_m and $a_{m/s}$ are the lattice constants of the primitive cell of various metals and the constructed M/S heterojunction, respectively. (h_1,h_2,h_3) is the crystalline index of contact surfaces of the metals, which is chosen due to low surface free energy and thermodynamic stability. W_m is the work function (in the unit of eV) of freestanding metals, which is calculated by the slab model using the ghost-atom method. ε is the strain applied to the metal to match the lattice of the semiconductor. E_b is the binding energy (in the unit of meV/Å^2) of M/S junctions. d_{ID} is the interfacial distance (in the unit of Å) of M/S junctions. ϕ_{TB} and W_B are the tunneling barrier height (in the unit of eV) and width (in the unit of eV), respectively. The

interface dipole $\Delta V = W_{s|m} - W_{m|s}$ (in the unit of eV) is the result of charge redistribution at the M/S interface, where $W_{s|m}$ and $W_{m|s}$ are the work function of semiconductor surface covered with metal and metal surface covered with semiconductor, respectively. ϕ_n and ϕ_p are the Schottky barriers (in the unit of eV) for electrons and holes of the M/S junctions, respectively. E_g is the band gap (in the unit of eV) of the semiconductor covered with metal.

Clean contacts in 2D/, semimetal/, and $Ti_3C_2T_2/MoGe_2N_4$ junctions

Metal	**NbS_2**	**$NbSe_2$**	**Gr**	**Bi**	**Sb**	**$Ti_3C_2(OH)_2$**	**$Ti_3C_2F_2$**	**$Ti_3C_2O_2$**
a_m	3.345	3.474	2.466	4.593	4.348	3.092	3.079	3.039
(h_1,h_2,h_3)	(0001)	(0001)	(0001)	(0001)	(0001)	(0001)	(0001)	(0001)
$a_{m/s}$	9.079	6.053	9.079	8.007	9.079	3.026	3.026	3.026
W_m	5.91	5.48	4.52	4.01	4.16	0.83	4.86	6.21
ε**(%)**	2.58	0.58	2.37	0.64	4.40	2.13	1.73	0.42
E_b	-28.59	-34.61	-17.52	-21.55	-17.14	-96.52	-50.85	-60.47
d_{ID}	3.05	3.08	3.19	3.24	3.16	1.76	2.33	2.37
ϕ_{TB}	5.26	4.80	4.21	3.65	3.81	1.14	3.86	4.69
W_B	1.88	1.80	1.77	1.78	1.77	0.77	1.30	1.37
ΔV	-0.30	-0.03	0.28	0.75	0.60	3.50	0.30	-0.58
ϕ_n	0.85	0.65	0.09	-0.08	-0.05	-0.46	0.27	0.8
ϕ_p	0.03	0.23	0.83	1.06	1.01	1.44	0.63	-0.09
E_g	0.88	0.88	0.92	0.98	0.96	0.98	0.90	0.71

Table S3. DFT calculated interfacial quantities for clean contacts in 2D/, semimetal/, and $Ti_3C_2T_2/MoGe_2N_4$ junctions. The terms follow the same definition as that of Table S2.

Metal	**Au(111)**	**Ag(111)**	**Cu(111)**	**Pd(111)**	**Ti(0001)**	**Sc(0001)**	**Pt(111)**	
T_{B}**(%)**	17.11	24.45	29.58	18.15	91.60	100.00	6.73	
ρ_T	0.079	0.057	0.043	0.068	0.012	0	1.20	
Metal	**NbS_2**	**$NbSe_2$**	**Gr**	**Bi(0001)**	**Sb(0001)**	**$Ti_3C_2(OH)_2$**	**$Ti_3C_2F_2$**	**$Ti_3C_2O_2$**
T_{B}**(%)**	1.21	1.78	2.42	3.07	2.90	43.37	7.30	4.78
ρ_T	3.93	2.89	2.44	2.26	2.27	0.035	1.21	1.22

Table S4. DFT calculated interfacial tunneling efficiency for metal/$MoGe_2N_4$ contacts. T_B is the tunneling probability across the interface estimated by using the rectangular barrier approximation. ρ_T is the tunneling-specific resistivity (in the unit of 10^{-9} Ω·cm^2) estimated by using the Simmon's model (see Methods).

Hydrogen-bonding contacts in MXene/MoS_2 junctions

M/MoS_2	**$Ti_3C_2(OH)_2$**	**$Nb_2C(OH)_2$**	**$Nb_4C_3(OH)_2$**	**$Ta_2C(OH)_2$**	**$Zr_2N(OH)_2$**	**$Hf_2N(OH)_2$**
a_m	3.092	3.214	3.171	3.202	3.283	3.266
$a_{m/s}$	3.182	3.182	3.182	3.182	3.182	3.182
$W_m + \Delta V$	4.10 (4.14)	4.08	3.95	4.14	3.97	4.01
ε**(%)**	2.83 (2.43)	0.99	0.35	0.62	3.08	2.57
E_b	-59.97 (-61.48)	-71.20	-68.87	-74.47	71.63	78.07
d_{ID}	2.18 (2.21)	2.09	2.10	2.04	2.08	2.03
ϕ_{TB}	2.06 (2.06)	1.73	1.80	1.55	1.66	1.45
W_B	1.77 (1.77)	1.03	1.08	0.98	1.01	0.89
T_B**(%)**	7.40	24.85	22.68	28.52	26.36	33.35
ρ_T	2.28	0.067	0.075	0.058	0.063	0.047
ϕ_n	-0.07 (-0.07)	-0.15	-0.16	-0.13	-0.15	-0.13
ϕ_p	1.85 (1.80)	1.86	1.87	1.85	1.87	1.85
E_g	1.78 (1.73)	1.71	1.71	1.72	1.72	1.72

Table S5. DFT calculated interfacial quantities for various MXene/MoS_2 junctions. The terms follow the same definition as that of Table S2 and S4. The lattice constant and work function of monolayer 2H-MoS_2 is calculated as 3.182 Å and 4.89 eV. The results calculated in this work by using the LCAO-PseudoDojo method in QuantumATK are in good agreement with the reported values (marked with parentheses) in ref. 23 by using the plane wave basis set combined with the projected augmented wave (PAW) method in VASP. Notably the phonon band structure indicates that $Nb_2C(OH)_2$ and $Ta_2C(OH)_2$ are predicted to be dynamically unstable. ρ_T of $Hf_2N(OH)_2/MoS_2$ is the smallest, corresponding to the smallest vdW gap.

Hydrogen-bonding contacts in various 2D M/S junctions

M/S	$Ti_3C_2(OH)_2$ /WGe_2N_4	$Ti_3C_2(OH)_2$ /$ZrSi_2N_4$	$Ti_3C_2(OH)_2$ /AlN	$Ti_3C_2(OH)_2$ /GaN	$Ti_3C_2(OH)_2$ /Ti_2CO_2	$Ti_3C_2(OH)_2$ /Al_2O_2	$Ti_3C_2(OH)_2$ /In_2O_2
a_s	3.026	3.040	3.130	3.224	3.032	2.955	3.451
W_s	4.97	6.18	3.64	4.18	5.91	4.43	6.51
χ	4.35	5.38	1.85	3.03	5.75	3.79	6.31
$a_{m/s}$	3.026	3.040	3.130	3.224	3.032	2.955	5.978
ε**(%)**	2.13	1.67	1.23	2.08	1.94	2.26	3.33
d_{ID}	1.80	1.67	1.94	1.91	1.40	1.71	1.40
ΔV	3.13	4.51	1.01	1.43	5.13	2.67	4.10
$\phi_{TB}, \phi_{TB}^{'}$	1.10, 0	1.63, 0.50	0, 0	0.22, 0	2.48, 0	1.19, 0	1.84, 0.34
$W_B, W_B^{'}$	0.77, 0	0.85, 0.34	0, 0	0.36, 0	1.5, 0	0.79, 0	1.11, 0.27
T_B**(%)**	43.73	25.64	100	84.14	8.87	41.52	25.96
ρ_T	0.035	0.056	0	0.020	1.95	0.037	0.092
ϕ_n	-0.29	-0.05	-0.41	-0.76	-0.26	-0.29	-1.31
E_g	1.26	1.76	3.68	2.84	0.34	1.35	0.43

M/S	$Ti_3C_2(OH)_2$ /CrO_2	$Ta_2C(OH)_2$ /Si_2F_2	$Ti_3C_2(OH)_2$ /$ZrCl_2$	$Ti_3C_2(OH)_2$ /GeS	$Ti_3C_2(OH)_2$ /GeSe	$V_2C(OH)_2$ /$MoSi_2N_4$	$Zr_2C(OH)_2$ /WSe_2
a_s	2.620	3.965	3.412	3.488	3.664	2.913	3.317
W_s	7.19	6.17	3.59	4.98	4.82	4.64	4.24
χ	6.99	5.77	3.10	3.74	3.67	3.79	3.44
$a_{m/s}$	5.239	7.930	5.910	6.042	6.264	2.913	3.317
ε**(%)**	2.17	3.07	4.43	2.30	1.29	2.97	0.02
d_{ID}	1.52	1.41	1.99	1.94	2.01	1.85	2.26
ΔV	5.57	4.55	2.21	2.60	2.71	2.48	2.47
$\phi_{TB}, \phi_{TB}^{'}$	2.55, 0.61	1.80, 0.50	0.86, 0	1.89, 0	1.82, 0.37	0.60, 0	1.63, 0
$W_B, W_B^{'}$	1.03, 0.45	0.91, 0.34	0.76, 0	1.05, 0	1.11, 0.29	0.57, 0	1.12, 0

T_B**(%)**	13.28	22.46	48.60	22.90	17.23	63.48	23.04
ρ_T	0.091	0.063	0.036	0.071	0.093	0.024	0.080
ϕ_n	-0.30	-0.78	-0.05	-0.42	-0.42	-0.32	-0.07
E_g	0.52	0.61	0.83	1.98	1.43	1.71	1.57

Table S6. DFT calculated interfacial quantities for various 2D Hydrogen-bonding M/S junctions. a_s is the lattice constant of the primitive cell of various semiconductors. W_s, and χ are the work function and electron affinity of the semiconductor, respectively. The terms follow the same definition as that of Table S2 and S4. In some systems the hydroxyl group in MXene forms an additional intralayer tunneling barrier ($\phi_{TB}^{'}, W_B^{'}$) (Fig. S19) due to tensile strain during heterojunction construction, which can essentially be removed in a larger model. Here, the total tunneling probability T_B is calculated as the product of these two tunneling probabilities.